文章编号： 1007-8827(2016)03-0352-11

多孔掺磷碳纳米管：磷酸水热合成及其在氧还原和锂硫电池中的应用

郭梦清[1]， 黄佳琦[1]， 孔祥屹[1]， 彭翊杰[1]，
税 晗[1]， 钱方圆[1]， 朱 林[1,2]， 朱万诚[2]， 张 强[1]
(1. 清华大学 化学工程系,绿色反应工程与工艺北京市重点实验室, 北京 100084;
2. 曲阜师范大学 化学工程系,山东 曲阜 273165)

摘 要： 碳纳米管优异的物理性质和可调的化学组成使其拥有广泛的应用前景。采用低温过程在碳骨架中引入磷原子预期带来可调的化学特性。本研究采用 170 ℃下水热处理碳纳米管-磷酸混合物获得磷掺杂的碳纳米管。磷掺杂的碳管的磷含量为 1.66%,比表面积为 132 m^2/g,热失重峰在纯氧环境下提升至 694 ℃。当掺磷碳纳米管用于氧还原反应时,其起始电位为−0.20 V,电子转移数为 2.60,反应电流显著高于无掺杂的碳纳米管。当其用作锂硫电池正极导电材料时,电极的起始容量为 1 106 mAh/g,电流密度从 0.1 C 提升至 1 C 时容量保留率为 80%,100 次循环的衰减率为每圈 0.25%。

关键词： 碳纳米管; 氧还原反应; 锂硫电池; 磷掺杂
中图分类号： TB332 **文献标识码：** A

基金项目:国家自然科学基金 (21306103, 21422604);国家重大科学研究计划(2015CB932500).
通讯作者:黄佳琦,博士,副研究员. E-mail: jqhuang@ tsinghua. edu. cn;
张 强,博士,副教授. E-mail: zhang-qiang@ mails. tsinghua. edu. cn
作者简介:郭梦清,博士生. E-mail: guo. 761@ osu. edu

Hydrothermal synthesis of porous phosphorus-doped carbon nanotubes and their use in the oxygen reduction reaction and lithium-sulfur batteries

GUO Meng-qing[1], HUANG Jia-qi[1], KONG Xiang-yi[1], PENG Hong-jie[1],
SHUI Han[1], QIAN Fang-yuan[1], ZHU Lin[1,2], ZHU Wan-cheng[2], ZHANG Qiang[1]
(1. *Beijing Key Laboratory of Green Chemical Reaction Engineering and Technology, Department of Chemical Engineering, Tsinghua University, Beijing* 100084, *China*;
2. *Department of Chemical Engineering, Qufu Normal University, Qufu* 273165, *China*)

Abstract: The many uses of carbon nanotubes (CNTs) depend not only on their intrinsic physical properties, but also on their tunable chemical components. Exploring a low-temperature method for the incorporation of phosphorus atoms in the carbon framework is expected to change the chemical properties of CNTs. Here, phosphorus-functionalized CNTs (PCNTs) were prepared by the direct hydrothermal treatment of a CNT-H_3PO_4 mixture at 170 ℃. The PCNTs had a high phosphorus content of 1.66 at%, a specific surface area of 132 $m^2 \cdot g^{-1}$, and an improved thermal stability with a weight loss peak at 694 ℃ during oxidation in pure oxygen. They showed good electrocatalytic activity for the oxygen reduction reaction with an onset potential of 0.20 V vs Hg/Hg_2Cl_2, an electron transfer number of 2.60, and a larger current density as well as improved cyclic stability compared with pristine CNTs. PCNTs were also used as conductive scaffolds for the cathode in lithium-sulfur batteries. The cathode delivered an initial discharge capacity of 1 106 $mAh \cdot g^{-1}$, a capacity retention of 80% from 0.1 to 1.0 C, and a low decay rate of 0.25% per cycle during 100 cycles.

Keywords: Carbon nanotube; Oxygen reduction reaction; Lithium sulfur batteries; Phosphorous-doped carbon

Received date: 2016-05-10; *Revised date*: 2016-06-09
Foundation item: National Natural Scientific Foundation of China (21306103, 21422604); National Basic Research Program of China (2015CB932500).
Corresponding authors: HUANG Jia-qi, Ph. D, Associate Professor. E-mail: jqhuang@ tsinghua. edu. cn;
ZHANG Qiang, Ph. D, Associate Professor. E-mail: zhang-qiang@ mails. tsinghua. edu. cn
Author introduction: GUO Meng-qing, Graduate Student. E-mail: guo. 761@ osu. edu

English edition available online ScienceDirect (http://www. sciencedirect. com/science/journal/18725805).
DOI: 10. 1016/S1872-5805(16)60019-7

1 Introduction

The broad applications of sp^2 carbon (such as carbon nanotubes (CNTs) and graphene) in the area of supercapacitors, batteries, fuel cells, heterogeneous catalysis, drug delivery, sensors, water treatment, as well as composites strongly depend not only on their intrinsic physical properties derived from sp^2 bonding structure, but also on their tunable chemical components through heteroatom doping and surface modification. The incorporation of heteroatoms brings tunable electronic properties and therefore offers tunable chemical reactivities. Recently, the heteroatom-incorporated nanocarbon is widely considered as a potential platform for diverse applications in heterogeneous catalysis (e. g. selective oxidation of cyclohexane and H_2S, oxidative dehydrogenation, and hydrohalogenation)[1], electrocatalysis (e. g. oxygen reduction reaction (ORR)[2-4] and oxygen evolution reaction[5]), energy storage (e. g. supercapacitors[6], lithium ion batteries[7], and lithium-sulfur batteries[8]), as well as gas adsorption (e. g. CO_2 capture[9]).

Phosphorus is a nonmetallic chemical element that is essential for life. Vast majority of P-containing compounds are employed as fertilizers. Similar to N atoms, P atoms can serve as electron donors for carbon to induce a shift in the Fermi level to the conducting band. However, the size of P atom is much larger than that of N atom and thus it is difficult to substitute into graphitic honeycomb lattice. Therefore, P atoms are always bonding with O and/or C in the heteroatom incorporated frameworks. The introduction of P-containing functional groups into carbon matrix significantly improves the thermal stability of the carbon matrix[10-12]. Therefore, P doped graphene are employed as n-type semiconductor in an air-stable field effect transistors[13]. The electrical conductivity of the carbon based material are enhanced by several orders of magnitude with the P-doping. Furthermore, P-containing functional groups in carbon frameworks also bring pseudo-capacitance when it served as the electrodes for supercapacitors. With the content of pyrophosphates decreasing and the heterogeneity of phosphorus containing species increasing, the capacitance increases and the retention ratio of the capacitor is increased. Recently, it was also reported that a small amount of P doping may greatly improve the selectivity by suppressing the combustion of hydrocarbons in oxidative dehydrogenation with P-functionalized CNTs as catalyst. The P-doped carbon catalyst also afford excellent reactivity in the electrochemical reduction of oxygen in an alkaline medium[2-4, 7, 14, 15]. The well combination of P with N atoms in the nanocarbon framework also rendered the synergy effect, which further promoted the catalytic activity for ORR[16, 17]. Therefore, exploring the material chemistry and their potential applications of P incorporated carbon nanomaterials with controllable doping manner is highly required.

In most cases, the P-incorporated carbon was synthesized by the decomposition of triphenylphosphine[2-4, 7, 17], phosphorus oxychloride[11], and 1-butyl-3-methylimidazolium hexafluorophosphate[14]. In addition, the chemical activation of carbon precursors with H_3PO_4 at a high temperature of 500 to 1 000 ℃ is also an efficient route to incorporate P into the framework of nanocarbon materials[6, 15, 16, 18-25]. However, the reduced P was exhausted as by products or wastes. A low temperature route for direct P-doping in carbon matrix is more favorable and environmental friendly to tune the surface chemistry of carbon materials towards unique properties and diverse applications.

In this contribution, a moderate hydrothermal modification strategy was proposed to synthesize phosphorous-functionalized carbon nanotubes (PCNTs). CNTs were selected as nanocarbon platform in this work because of their extraordinary intrinsic properties, easiness for structural characterization, as well as their broad applications. The CNTs have been mass produced through fluidized bed chemical vapor deposition at a low cost and have been commercialized as conductive agents for lithium-ion batteries and additives for tires or plastics. We employed the idea of hydrothermal modification of CNTs at a low temperature of 170 ℃. The as-obtained PCNTs were with a P content of 1. 66 at%. The electrochemical performance was evaluated as the electrocatalyst for ORR and conductive scaffolds for lithium-sulfur batteries.

2 Experimental

2.1 Synthesis of CNTs and PCNTs

The CNTs were synthesized in a 50 mm fluidized bed reactor on layered double hydroxide derived catalysts. The raw CNTs were routinely purified by HCl ($3.0\ mol\cdot g^{-1}$) and subsequent NaOH ($15.0\ mol\cdot g^{-1}$) aqueous solution to remove the catalyst residual. The PCNTs were fabricated by hydrothermal functionaliza-

tion with H_3PO_4 as the phosphorus source. H_3PO_4 (85%) and CNTs were well mixed in a Teflon-lined stainless steel autoclave with a mass ratio of 6.78, corresponding to the mass ratio of the P element to CNTs of 2.0∶1.0. The H_3PO_4/CNT mixture was sealed and heated to 170 ℃ at a ramp rate of 0.5 ℃/min. The hydrothermal treatment was kept at 170 ℃ for 12.0 h and then the autoclave was cooled down to room temperature naturally. The solid products were further rinsed by deionized water to pH = 7.0 and then dried at 110 ℃ for 6.0 h. Finally, the PCNTs were collected for further structure characterization and performance evaluation.

2.2 Structure characterization

The nanostructures of CNTs and PCNTs were characterized by a JSM 7401F scanning electron microscope (SEM) and a JEM 2010 transmission electron microscope (TEM). The Raman spectra were collected with a Horiba Jobin Yvon LabRAM HR800 Raman spectrometer with a He-Ne laser excited at 633 nm. The N_2 sorption isotherms of CNTs and PCNTs were collected by the Autosorb-IQ_2-MP-C system. Before measurements the sample was degassed at 200 ℃ until a manifold pressure of 2 mm Hg was reached. The specific surface areas (SSAs) of the CNT samples were calculated from the isotherm by the Brunauer-Emmett-Teller (BET) equation. The pore size distribution was determined by the non-linear density functional theory model. The thermogravimetric (TG) analysis of the CNT samples was performed by the Mettler Toledo TGA/DSC-1 under O_2 atmosphere at a ramping rate of 20 ℃/min. The P and O-containing functional groups were characterized by X-ray photoelectron spectroscopy (XPS) on an Escalab 250xi system. The XPS spectra were calibrated with a reference binding energy at 284.4 eV of C 1s peak. A Shirley background was subtracted prior to fitting. The peak areas were normalized with theoretical cross-sections to obtain the relative surface elemental compositions.

2.3 ORR performance of the CNTs and PCNTs

To evaluate the ORR performance, the CNTs and PCNTs were dispersed in ethanol (5.0 mg·mL^{-1}) as catalyst ink. The CNT sample was then transferred onto the glass carbon electrode via a routine drop casting with an areal loading amount of 0.25 mg·cm^{-2}. After the evaporation of ethanol at room temperature, a drop of Nafion solution (1.0 wt%) was cast onto the surface of the electrode to form a thin layer and then dried in an oven at 60 ℃ for 30 min to serve as the working electrode. The ORR measurements were performed in a three-electrode setup in a 0.10 mol·L^{-1} KOH aqueous electrolyte. The saturated calomel electrode was used as the reference electrode, and Pt foil was employed as the counter electrode. The cyclic voltammogram (CV) profiles were collected at a scan rate of 100.0 mV·s^{-1} on the CHI 760D electrochemical workstation.

$$\frac{1}{J}=\frac{1}{B\omega^{1/2}}+\frac{1}{J_K} \tag{1}$$

$$B=0.20nFC_0D_0^{2/3}\nu^{-1/6} \tag{2}$$

Where J is the measured current density, B is the Levich constant, ω is the angular velocity ($\omega = 2\pi N$, N is the linear rotation rate), J_K is the kinetic current density, n is the overall number of electrons transferred in the ORR, F is the Faraday constant (96 485 C·mol^{-1}), C_0 is the bulk concentration (1.2×10^{-3} mol·g^{-1}) of O_2, D_0 is the diffusion coefficient (1.9×10^{-5} cm^2·s^{-1}) of O_2 in the KOH solution, and ν is the kinetic viscosity (0.01 cm^2·s^{-1}) of the electrolyte solution[3].

2.4 CNT and PCNT based cathodes for lithium-sulfur batteries

The C/S composite electrode was fabricated by mixing PCNTs and sulfur powder by ball-milling, followed by co-heating in a sealed container at 155 ℃ for 2.0 h, which was similar to our recent works[26]. The sulfur content is 55 wt% after the heat treatment. Later on, a slurry was made by mixing the PCNT@S composite with PVDF binder and CNT conductive agent in NMP with a mass ratio of PCNT@S∶PVDF∶CNTs = 85∶10∶5. The mixture was vigorously magnetic stirred for about 12.0 h to obtain a homogeneously mixed slurry. The as-obtained slurry was coated on an Al foil and then dried in a vacuum drying oven at 60 ℃ for 6.0 h. After these procedures, the coated Al foil was punched into disks with a diameter of 13 mm for the working electrodes. The electrodes were assembled in a two-electrode cell configuration using standard 2025 coin-type cells vs 1.0 mm thick Li metal foil as counter/reference electrodes. 1,3-dioxolane: 1,2-dimethoxyethane (v/v = 1/1) with 1.0 mol·g^{-1} lithium bis(trifl uoromethanesulfonyl) imide was selected as the electrolyte. The Celgard 2400 polypropylene membrane was employed as the separator. An Ar-filled glove box equipped with a purifying system (oxygen and water content below 1 ppm) was used to prepare and assemble the coin-type cells based on CNT electrodes. The sulfur loading on each electrode was around 1.3 mg·cm^{-2}. The as-obtained coin cells were tested in galvanostatic mode at 25 ℃ within a voltage range of 1.0-3.0 V by the Neware multichannel battery cyclers.

3 Results and discussion

3.1 Physical characteristics of PCNTs

The raw CNTs grown in a fluidized bed reactor were entangled with each other (Fig. 1a). After the hydrothermal reaction with H_3PO_4, the PCNTs were still with the agglomerated morphology (Fig. 1b). The diameter of the raw CNTs ranged from 8 to 15 nm. Some amorphous carbon was decorated on the outer wall of raw CNTs (Fig. 1c), which was hardly detected after chemical modification with H_3PO_4 (Fig. 1d). Although the P-containing functional groups were grafted on the surface, the sp^2-conjunction structure of inner walls was well preserved. Raman spectra of CNT samples are presented in Fig. 2a. Two typical peaks centered at about 1 350 cm^{-1} (*D* band) and 1 590 cm^{-1} (*G* band) were resolved for both samples, which were associated to the E_{2g} phonon of sp^2 C atoms and breathing mode of *k* point of phonons of A_{1g} symmetry, respectively. The I_D/I_G ratios were 1.67 and 1.44 for CNTs and PCNTs, respectively, which were indicators of the disorder degree in the graphite derivatives. The drop of the I_D/I_G ratio was attributed to the removal of attached amorphous carbon on CNTs during the hydrothermal functionalization with H_3PO_4, which was in consistence with the high resolution TEM images shown in Fig. 1. The robust sp^2-conjuncted frameworks were well preserved while the disordered carbon impurity was eliminated. Meanwhile, both *D* band and *G* band of PCNTs manifested a blue shift, suggesting the P-doping and its related impact on photon diffraction behavior.

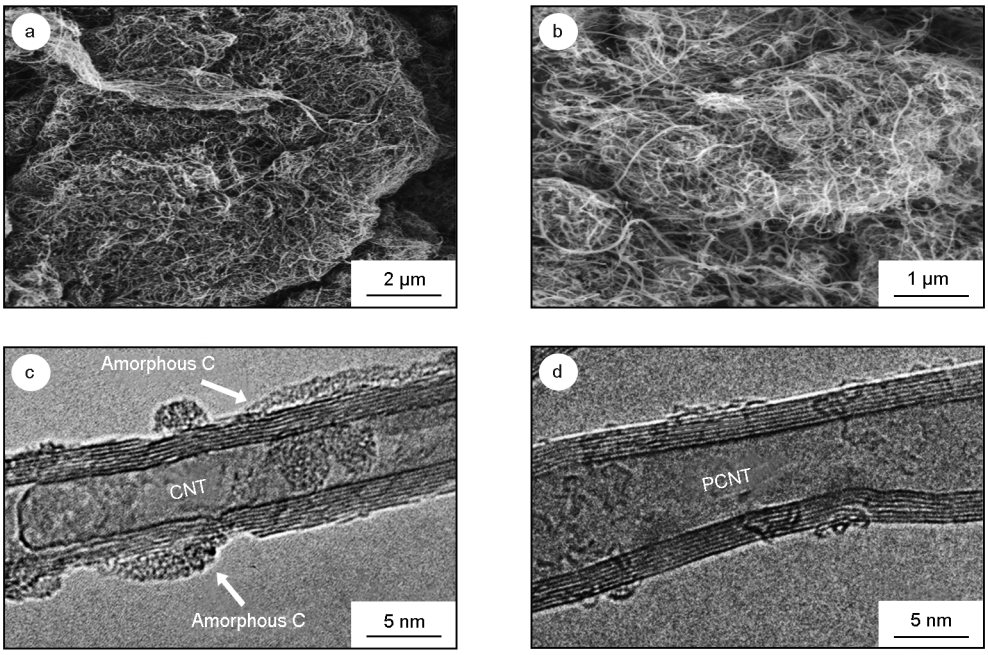

Fig. 1　SEM images of (a) CNTs and (b) PCNTs; high resolution TEM images of (c) CNTs and (d) PCNTs.

The thermal oxidation property of PCNTs was investigated by TG analysis. As shown in Fig. 2b, the weight loss peaks of CNTs and PCNTs were located at 569 and 694 ℃, respectively. Such shift was attributed to the removal of thermally-unstable amorphous carbon and the fire retardation effect derived from phosphorus containing groups, which has been widely reported by the carbon community[10-12]. This was also in good accordance with the recent reported graphene phosphoric acid as an efficient flame retardant[27]. The enhanced oxygen durability might benefit the applicable potential for oxidation-involving heterogeneous catalysis. However, the weight loss onset point shifted to low temperature for the PCNTs, which is induced by the loss of unstable heteroatoms absorbed on the CNT surface.

The porous texture of the CNTs and PCNTs were further evaluated by the N_2 isothermal sorption (Fig. 2c). After hydrothermal modification, the BET SSA of CNT samples decreased from 249 to 132 $m^2 \cdot g^{-1}$. The pores with a size over 20 nm contributed more than 95% of the total pore volume (Fig. 2d). Compared to raw CNTs, PCNTs possessed greatly a decrease in volume of pores with a size less than 10 nm, which was ascribed to the removal of highly disorder carbon impurities with much more edges and defects.

Some CNTs preferred to attach with each other due to the capillary forces during the drying process. The decline of the SSA was quite different from the chemical activation with lignin materials with H_3PO_4, which will be explained in the following section.

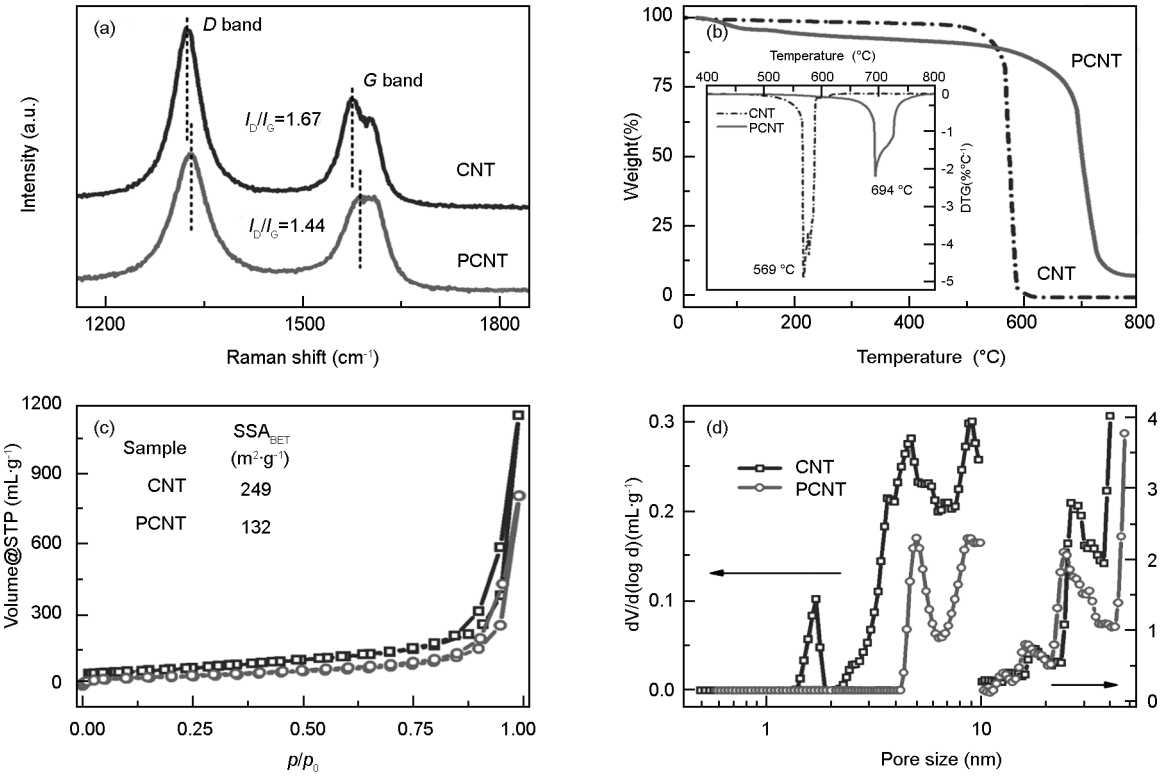

Fig. 2 (a) Raman spectra and (b) TG profiles of CNTs and PCNTs; (c) N_2 sorption isotherms, BET SSA (SSA_{BET}); (d) pore size distributions of CNT samples.

3.2 The functional groups on PCNTs

The functional groups on the surface of PCNTs were investigated by XPS (Fig. 3). The relative abundance of C, O, and P elements was calculated accordingly (Table 1). After the H_3PO_4 modification, the P content in PCNTs was increased to 1.66 at% (Fig. 3a), and the amount of oxygen increased from 1.40 to 6.98 at%. The C/O atomic ratio decreased from 70.4 to 13.1. The detailed O- and P-containing functional groups were further determined by peak fitting O 1s (Fig. 3b,d) and P 2p (Fig. 3c) spectra. The assignment and quantification of O and P components were summarized in Table 2 and 3, respectively. The high resolution C1s peaks for all samples were centered at 284.6 eV with a tail toward high binding energy. The fitting of the O1s spectra was resolved into five individual component peaks representing O1 (530.4 eV)-quinones, O2 (531.2 eV)—COOH/C(O)O, O3 (531.9 eV)— C═O , O4 (532.8 eV) —C—O, and O5 (533.4 eV)—OH. The fitting of the P 2p spectra was resolved into three individual component peaks representing P1 (133.8 eV) —P—C, P2 (134.6 eV)—P—O, and P3 (135.5 eV)— P═O [24]. The full width at half maximum for O and P peak fitting was 1.5 and 1.3 eV, respectively. As shown in Table 3, there were mainly O3 (— C═O), O4 (—C—O), and O5 (—OH) functional groups on the CNTs. The O content groups (O2-O5) increased in proportion with H_3PO_4 modification. The relative ratio of —OH group decreased together with the rise of —C—O group, indicating the dehydration reaction during the hydrothermal modification. Meanwhile, all the P-containing functional groups increased. Nevertheless, the —P—O groups were the dominant contribution in PCNTs. The phosphoric acid can easily attack the point defects, edge of sp^2 nanotubes layers, and O-containing functional groups (especially for the —OH groups). As a result, —P—O— was formed in the PCNTs. The — P═O was detected mainly from phosphoric acid. There were —P—C groups in the PCNTs, which was attributed to the dehydration reaction between phosphoric acid and carbon support.

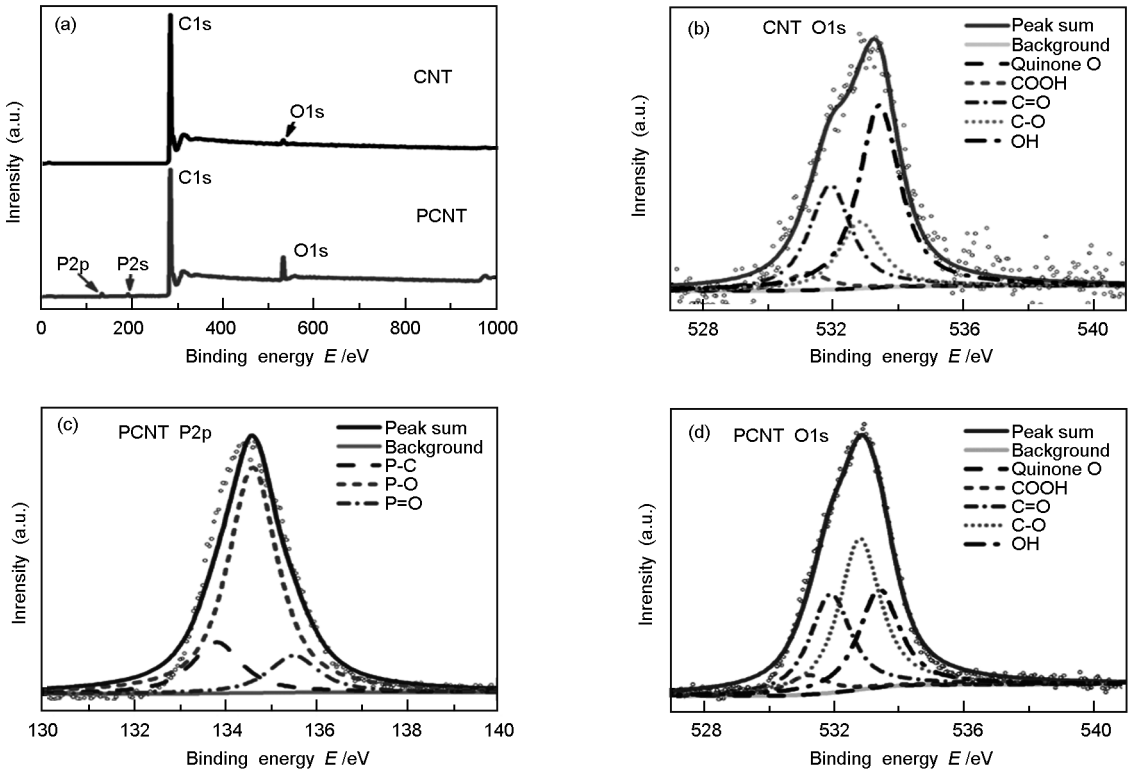

Fig. 3　The functional groups on CNTs and PCNTs: (a) overall XPS spectra, (b) XPS spectra of CNTs (upper) and PCNTs (below) in O 1s region, and (c) P 2p region for PCNTs.

Table 1　The surface elements of CNTs and PCNTs determined by XPS analysis.

Samples	C (at%)	O (at%)	P (at%)	C/O ratio
CNTs	98.60	1.40	–	70.4
PCNTs	91.36	6.98	1.66	13.1

Table 2　The oxygen containing functional groups on CNTs and PCNTs.

Samples (at%)	O1 (530.4 eV)	O2 (531.2 eV)	O3 (531.9 eV)	O4 (532.8 eV)	O5 (533.4 eV)
CNTs	0.00	0.06	0.40	0.25	0.69
PCNTs	0.00	0.40	2.03	3.10	2.01

Table 3　The phosphorous containing functional groups on PCNTs.

Samples (at%)	P1 (133.8 eV)	P2 (134.6 eV)	P3 (135.5 eV)
PCNTs	0.27	1.19	0.19

3.3　Proposed formation mechanism

The chemical activation of biomass with H_3PO_4 has been widely explored for activated carbon formation[18, 19, 23, 28, 29]. The dehydration of H_3PO_4 at high temperature to hemicelluloses and lignin is the dominant chemical reaction. Then pyrophosphoric acid as well as phosphoric acid inserts the carbon to prop up the space, which delivers high SSA value[28, 29].

In contrast, there are very limited —OH groups on the surface of the CNTs. Consequently, the dehydration reaction is not dominant. A two-step modification mechanism was proposed as follows: Firstly, H_3PO_4 preferred to attack the edges or defect sites on CNTs, especially the edge of amorphous carbon on the outer wall of CNTs, which had been well confirmed by the TEM image and Raman spectra. This induced the rise of oxygen-containing functional groups on the surface of CNTs. Secondly, H_3PO_4 further attacked —OH on the surface of CNTs to form ester bond (—P—O—C—) by dehydration reaction (Fig. 4). Since dehydration reactions were not the dominant, H_3PO_4 chemical activation created few micropores compared with KOH activation. Actually,

the reaction between H_3PO_4 and disordered carbon impurities healed the defects of CNTs instead. Therefore, the SSA of PCNTs was only 132 $m^2 \cdot g^{-1}$. Similar to the hydrothermal carbonization of biomass into doped carbon at a mild temperature of less than 200 ℃[30], the hydrothermal modification strategy reported herein can be applied as a versatile method in carbon nanomaterial functionalization for a facile, low-cost, environmentally friendly, and nontoxic route.

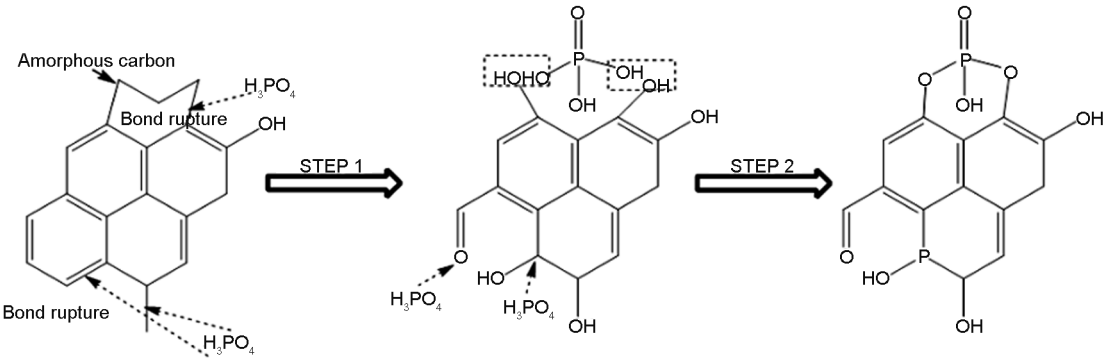

Fig. 4 The proposed mechanism for hydrothermal functionalization of PCNTs from CNTs.

The P-containing functional groups introduced the unique interfaces of carbon supports with absorbed molecules such as O_2 and sulfur species. As an electron-donor, both P and O atoms can tune the electron density on CNT surface. Therefore, the as-obtained PCNTs were considered as potential high performance ORR catalysts and carbon scaffolds for lithium-sulfur batteries.

3.4 PCNTs as catalysts for oxygen reduction reactions

The PCNTs can serve as metal-free catalysts with a high electrocatalytic activity for ORR. The sluggish ORR at the cathode of fuel cells and metal-air batteries requires efficient catalysts. The Pt based noble metal catalysts have been widely applied as high performance catalysts. However, the high cost, low abundance, crossover effect, and CO poisoning of Pt and Pt alloys hinders its practical applications. The reducing/replacing of noble metal with doped carbon nanomaterials has been highly interested recently[2-4, 7, 14-17, 31, 32]. Herein, PCNTs synthesized by the hydrothermal route were employed as the catalysts for ORR.

Fig. 5a presents the CV curve of PCNTs in 0.10 M KOH saturated with oxygen at a scan rate of 100 $mV \cdot s^{-1}$. When the potential of the working electrode decreased to the onset potential at −0.20 V, the oxygen in the solution began to be reduced, enhancing the current density on the electrode. When the potential was lower than −0.40 V, due to the consumption in the reaction, the concentration of O_2 in the solution decreased, weakening the current density. Therefore, an obvious ORR peak was observed around −0.33 V. Fig. 5b illustrates the linear sweep voltammogram (LSV) for both CNTs and PCNTs in 0.10 M KOH saturated with O_2 at a rotation rate of 1 600 r/min. When the potential was lower than −0.20 V, ORR began to take place. The reaction was kinetic-limited while the potential decreased from −0.30 to −0.90 V. As the potential of the working electrode decreased to −0.90 V, mass transfer became the rate-limiting step. Therefore, the current density of the working electrode merely increased after reaching diffusion-limited current. Compared with raw CNT electrode, PCNTs exhibited higher current density and reduced potential barrier, indicating an improved electrochemical reactivity of PCNT catalyst for ORR.

A family of LSV profiles were available and the Koutecky-Levich plots of PCNTs and CNTs at −0.6 V are shown in Fig. 5c. A linear relationship was illustrated, from which the electron transfer number was fitted as 2.36 and 2.60 for CNTs and PCNTs, respectively. If the oxygen was reduced through a two-electron pathway, the oxygen would be reduced to peroxide first, and then the peroxide would be further reduced to OH^-. The peroxides produced in the two-electron pathway caused degradation of the membrane and catalyst, resulting in declining cell performance in fuel cells. In contrast, the oxygen was directly reduced to OH- (four-electron pathway), which was preferred for ORR in fuel cells and metal-air batteries. Compared with CNTs, the PCNTs manifested a larger portion of four-electron pathway in ORR.

The chronoamperometric durability tests were also performed at a constant voltage of −0.3 V in a 0.1 $mol \cdot g^{-1}$ KOH solution saturated with O_2 at a rotating rate of 1 600 r/min. As shown in Fig. 5d, the

relative current of CNT electrode reduced to 64%, while PCNT electrode delivered a 70% retention after a 9 000 s test. This indicated that the stability of CNT catalyst was improved after the modification with H_3PO_4. The most possible reason was enhanced oxygen durability of PCNTs as TG analysis indicated.

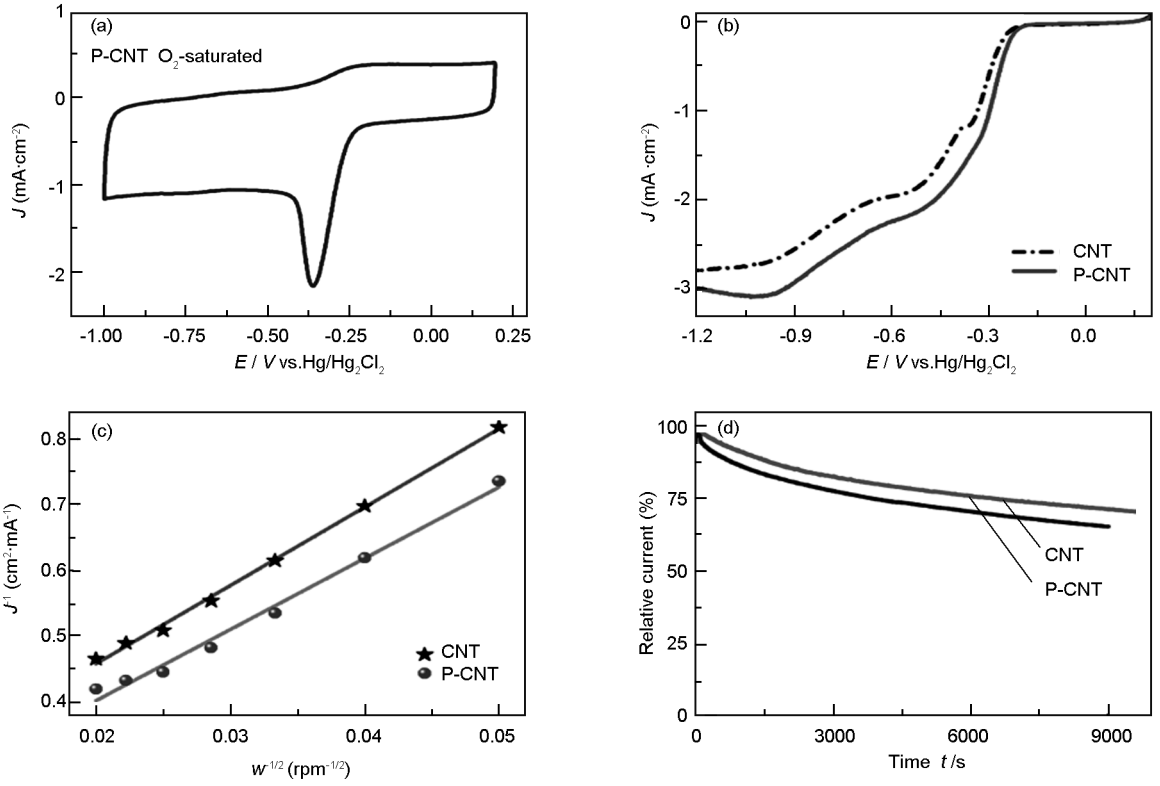

Fig. 5　The ORR performance of PCNT and CNT electrode:
(a) CV curve of ORR of PCNTs at a scan rate of 100 $mV \cdot s^{-1}$ in O_2-saturated 0.1 M KOH solution;
(b) LSV curves of the samples at a scan rate of 5 $mV \cdot s^{-1}$ and a rotation rate of 1 600 r/min in O_2-saturated 0.1 M KOH solution;
(c) Koutecky-Levich plots of PCNT and CNT electrodes at −0.6 V;
(d) The durability evaluation of PCNT and CNT electrodes at −0.3 V with a rotating rate of 1 600 r/min.

3.5　The PCNTs as carbon scaffolds for lithium-sulfur batteries

To meet the rising requirement of energy storage systems in high energy density, lithium-sulfur batteries attract great interests recently owing to a high theoretical capacity of sulfur (1 672 $mA \cdot g^{-1}$) and a high theoretical energy density of lithium-sulfur redox (2 500 $Wh \cdot kg^{-1}$), significantly surpassing conventional lithium ion batteries. In addition, the sulfur also shows advantages in its high natural abundance on earth, high environmental benign property, as well as low cost. However, the insulate nature of both sulfur and Li_2S, the volume changes during cycling, as well as the unexpected shuttle of polysulfide intermediates hinder the use of sulfur cathode with a superb efficiency and stable cycling[33-39]. The incorporation of conductive carbon host is an effective route to improve the conductivity of electrodes while limiting the dissolution of polysulfide intermediates[33-39]. In this contribution, PCNTs were employed as the conductive cathode scaffolds to host sulfur for lithium-sulfur batteries.

Compared with cathode composed of CNTs and sulfur, the PCNT based electrode exhibited a significant promotion on discharge capacity, cycle stability, and coulombic efficiency (Fig. 6). When the charge/discharge current density was 0.1 C (1.0 C = 1 672 $mAh \cdot g^{-1}$), the PCNT and CNT based electrodes exhibited discharge capacities of 1 106 and 942 $mAh \cdot g^{-1}$, respectively. With the rise of the current density to 1.0 C, their discharge capacities dropped to 885 and 545 $mAh \cdot g^{-1}$ with a capacity retention of 80% and 58%, respectively. The cycling performance of PCNT and CNT based sulfur cathode at 0.2 C is demonstrated as Fig. 6b. The discharge capacity of PCNT and CNT based cathodes after 100 cycles remained a value of 917 and 646 $mAh \cdot g^{-1}$, respectively. Most significantly, the Coulombic efficiency of PCNTs was around 96% and remained constant during the 100 cycles. In contrast, the Coulombic efficiency of CNTs decreased drastically from 90% to 70%. Note that lithium anodes were both un-

protected. This dramatic improvement indicated a great depression on shuttle effect, suggesting the favorable interaction between sulfur species and P-functionalized carbon hosts. With the introduction of polar P containing groups on CNTs, polysulfide molecules would be preferentially adsorbed on the carbon scaffolds. The strong coupled interfaces between the carbon matrix and sulfur retarded the diffusion of polysulfides in the electrode and increased the utilization of sulfur in the cathode[8, 37, 38, 40-44]. However, the complex chemistry of polysulfides in the electrolyte and their irreversible deposition on the anode and other dead space in the cell induced the loss of discharge capacity. Both the Coulombic efficiency and cyclic performance can be further improved by ion selective separators[45], the anode protection (e. g. addition of $LiNO_3$ into the electrolyte[46]), or the incorporation of polymer chains[47], or porous polysulfide reservoirs[48] for the highly hydrophilic surface and a chemical gradient.

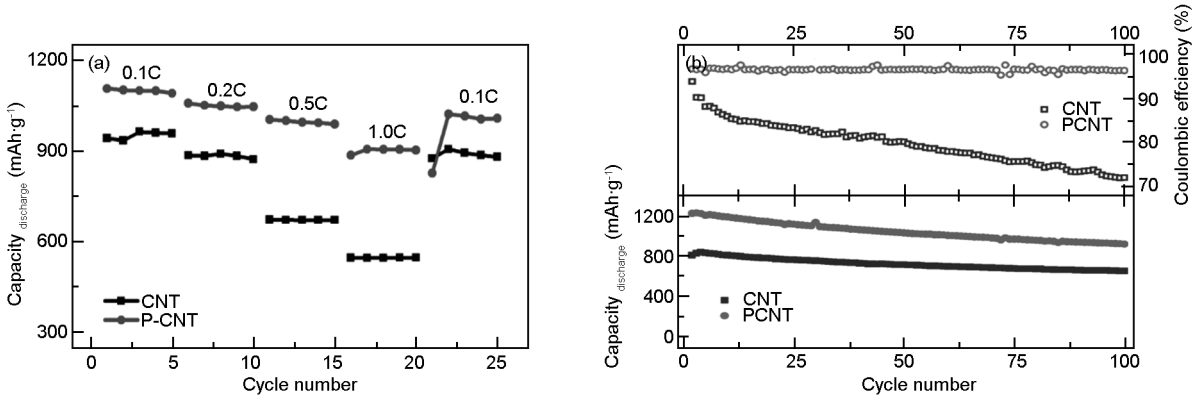

Fig. 6 The PCNT and CNT based cathodes for lithium-sulfur batteries: (a) The rate performance and (b) the cycling performance at a current rate of 0.2 C.

4 Conclusions

The porous P-functionalized CNTs were directly prepared through a mild hydrothermal treatment of CNT-H_3PO_4 mixture at 170 ℃. The as-obtained PCNTs exhibited a specific surface area of 132 $m^2 \cdot g^{-1}$, an improved oxygen durability with a weight loss peak at 694 ℃, and a high P content of 1.66 at%. When PCNTs were used as catalysts for ORR, they offered an onset potential of −0.2 V vs Hg/Hg_2Cl_2, an electron transfer number of 2.60, a larger current density, and an improved cycling stability compared with CNT catalysts. When PCNTs served as carbon scaffold for lithium-sulfur batteries, the as-obtained cells delivered a high initial discharge capacity of 1 106 $mAh \cdot g^{-1}$, a good rate retention of 80% from 0.1 to 1.0 C, a considerable capacity retention of 75% after 100 cycles, and especially a high and stable Coulombic efficiency over 96%. The P-functionalized CNTs are promising nanostructured carbon with tunable surface for heterogeneous catalysis, drug delivery, reactant reservoirs, and advanced energy storage.

References

[1] Su D S, Zhang J, Frank B, et al. Metal-free heterogeneous catalysis for sustainable chemistry[J]. ChemSusChem, 2010, 3: 169-180.

[2] Liu Z W, Peng F, Wang H J, et al. Phosphorus-doped graphite layers with high electrocatalytic activity for the O_2 reduction in an alkaline medium[J]. Angew Chem Int Ed, 2011, 50: 3257-3261.

[3] Yang D S, Bhattacharjya D, Inamdar S, et al. Phosphorus-doped ordered mesoporous carbons with different lengths as efficient metal-free electrocatalysts for oxygen reduction reaction in alkaline media[J]. J Am Chem Soc, 2012, 134: 16127-16130.

[4] Yang D S, Bhattacharjya D, Song M Y, et al. Highly efficient metal-free phosphorus-doped platelet ordered mesoporous carbon for electrocatalytic oxygen reduction[J]. Carbon, 2014, 67: 736-743.

[5] Tian G L, Zhao M, Yu D, et al. Nitrogen-doped graphene/carbon nanotube hybrids: In situ formation on bifunctional catalysts and their superior electrocatalytic activity for oxygen evolution/reduction reaction[J]. Small, 2014, 10: 2251-2259.

[6] Wang C, Sun L, Zhou Y, et al. P/N co-doped microporous carbons from H_3PO_4-doped polyaniline by in situ activation for supercapacitors[J]. Carbon, 2013, 59: 537-546.

[7] Zhang C Z, Mahmood N, Yin H, et al. Synthesis of phosphorus-doped graphene and its multifunctional applications for oxygen reduction reaction and lithium ion batteries[J]. Adv Mater, 2013, 25: 4932-4937.

[8] Song J X, Xu T, Gordin M L, et al. Nitrogen-doped mesoporous carbon promoted chemical adsorption of sulfur and fabrication of high- areal- capacity sulfur cathode with exceptional cycling stability for lithium- sulfur batteries[J]. Adv Funct Mater, 2014, 24: 1243-1250.

[9] Song J, Shen W Z, Wang J G, et al. Superior carbon-based CO_2 adsorbents prepared from poplar anthers[J]. Carbon, 2014, 69: 255-263.

[10] Strelko V V, Kuts V S, Thrower P A. On the mechanism of

possible influence of heteroatoms of nitrogen, boron and phosphorus in a carbon matrix on the catalytic activity of carbons in electron transfer reactions[J]. Carbon, 2000, 38: 1499-1503.
[11] Lee Y J, Radovic L R. Oxidation inhibition effects of phosphorus and boron in different carbon fabrics[J]. Carbon, 2003, 41: 1987-1997.
[12] Wu X X, Radovic L R. Inhibition of catalytic oxidation of carbon/carbon composites by phosphorus[J]. Carbon, 2006, 44: 141-151.
[13] Some S, Kim J, Lee K, et al. Highly air-stable phosphorus-doped n-type graphene field-effect transistors[J]. Adv Mater, 2012, 24: 5481-5486.
[14] Li R, Wei Z D, Gou X L, et al. Phosphorus-doped graphene nanosheets as efficient metal-free oxygen reduction electrocatalysts[J]. RSC Adv, 2013, 3: 9978-9984.
[15] Wu J, Yang Z R, Li X W, et al. Phosphorus-doped porous carbons as efficient electrocatalysts for oxygen reduction[J]. J Mater Chem A, 2013, 1: 9889-9896.
[16] Choi C H, Park S H, Woo S I. Binary and ternary doping of nitrogen, boron, and phosphorus into carbon for enhancing electrochemical oxygen reduction activity[J]. ACS Nano, 2012, 6: 7084-7091.
[17] Yu D S, Xue Y H, Dai L M. Vertically aligned carbon nanotube arrays co-doped with phosphorus and nitrogen as efficient metal-free electrocatalysts for oxygen reduction[J]. J Phys Chem Lett, 2012, 3: 2863-2870.
[18] Jagtoyen M, Derbyshire F. Activated carbons from yellow poplar and white oak by H_3PO_4 activation[J]. Carbon, 1998, 36: 1085-1097.
[19] Puziy A M, Poddubnaya O I, Martinez-Alonso A, et al. Synthetic carbons activated with phosphoric acid II. Porous structure[J]. Carbon, 2002, 40: 1507-1519.
[20] Kucukayan-Dogu G, Sen H S, Yurdakul H, et al. Synthesis of phosphorus included multiwalled carbon nanotubes by pyrolysis of sucrose[J]. J Phys Chem C, 2013, 117: 24554-24560.
[21] Zuo S L, Yang J X, Liu J L. Effects of the heating history of impregnated lignocellulosic material on pore development during phosphoric acid activation[J]. Carbon, 2010, 48: 3293-3295.
[22] Romero-Anaya A J, Lillo-Rodenas M A, de Lecea C S M, et al. Hydrothermal and conventional H_3PO_4 activation of two natural bio-fibers[J]. Carbon, 2012, 50: 3158-3169.
[23] Yue Z R, Economy J, Mangun C L. Preparation of fibrous porous materials by chemical activation 2. H_3PO_4 activation of polymer coated fibers[J]. Carbon, 2003, 41: 1809-1817.
[24] Zhao X C, Zhang Q, Zhang B, et al. Dual-heteroatom-modified ordered mesoporous carbon: Hydrothermal functionalization, structure, and its electrochemical performance[J]. J Mater Chem, 2012, 22: 4963-4969.
[25] Fan X, Yu C, Ling Z, et al. Hydrothermal synthesis of phosphate-functionalized carbon nanotube-containing carbon composites for supercapacitors with highly stable performance[J]. ACS Appl Mater Interfaces, 2013, 5: 2104-2110.
[26] Peng H J, Huang J Q, Zhao M Q, et al. Nanoarchitectured graphene/CNT@ porous carbon with extraordinary electrical conductivity and interconnected micro/mesopores for lithium-sulfur batteries[J]. Adv Funct Mater, 2014, 24: 2772-2781.
[27] Kim M J, Jean I Y, Seo J M, et al. Graphene phosphonic acid as an efficient flame retardant[J]. ACS Nano, 2014, 8: 2820-2825.
[28] Hayashi J, Kazehaya A, Muroyama K, et al. Preparation of activated carbon from lignin by chemical activation[J]. Carbon, 2000, 38: 1873-1878.
[29] Guo Y P, Rockstraw D A. Physical and chemical properties of carbons synthesized from xylan, cellulose, and kraft lignin by H_3PO_4 activation[J]. Carbon, 2006, 44: 1464-1475.
[30] Zhao L, Baccile N, Gross S, et al. Sustainable nitrogen-doped carbonaceous materials from biomass derivatives[J]. Carbon, 2010, 48: 3778-3787.
[31] Ramasahayam S K, Nasini U B, Bairi V, et al. Microwave assisted synthesis and characterization of silicon and phosphorous co-doped carbon as an electrocatalyst for oxygen reduction reaction[J]. RSC Adv, 2014, 4: 6306-6313.
[32] Jo G, Sanetuntikul J, Shanmugam S. Boron and phosphorous-doped graphene as a metal-free electrocatalyst for the oxygen reduction reaction in alkaline medium[J]. RSC Adv, 2015, 5: 53637-53643.
[33] Zhang Q, Cheng X B, Huang J Q, et al. Review of carbon materials for advanced lithium-sulfur batteries[J]. New Carbon Mater, 2014, 29: 241-264.
[34] Xu F, Tang Z W, Huang S Q, et al. Facile synthesis of ultra-high-surface-area hollow carbon nanospheres for enhanced adsorption and energy storage[J]. Nat Commun, 2015, 6: 7221.
[35] Shi J L, Tang C, Peng H, et al. 3D mesoporous graphene: CVD self-assembly on porous oxide templates and applications in high-stable Li-S batteries[J]. Small, 2015, 11: 5243-5252.
[36] TANG Zhi-wei, XU Fei, LIANG Ye-ru, et al. Preparation and electrochemical performance of a hierarchically porous activated carbon aerogel/sulfur cathode for lithium-sulfur batteries[J]. New Carbon Mater, 2015, 30: 319-326.
(唐志伟, 徐　飞, 梁业如, 等. 层次孔活性炭气凝胶/硫复合正极材料的制备及其电化学性能[J]. 新型炭材料, 2015, 30: 319-326.
[37] Zhou G M, Yin L C, Wang D W, et al. Fibrous hybrid of graphene and sulfur nanocrystals for high-performance lithium-sulfur batteries[J]. ACS Nano, 2013, 7: 5367-5375.
[38] Gu X X, Tong C J, Lai C, et al. A porous nitrogen and phosphorous dual doped graphene blocking layer for high performance Li-S batteries[J]. J Mater Chem A, 2015, 3: 16670-16678.
[39] Liang J, Sun Z H, Li F, et al. Carbon materials for Li-S batteries: Functional evolution and performance improvement[J]. Energy Storage Mater, 2016, 2: 76-106.
[40] Sun F G, Wang J T, Chen H C, et al. High efficiency immobilization of sulfur on nitrogen-enriched mesoporous carbons for Li-S batteries[J]. ACS Appl Mater Interfaces, 2013, 5: 5630-5638.
[41] Peng H J, Hou T, Zhang Q, et al. Strongly coupled interfaces between heterogeneous carbon host and sulfur-containing guest for highly-stable lithium-sulfur batteries: Mechanistic insight into capacity degradation[J]. Adv Mater Interfaces, 2014, 1: 1400227.
[42] Tang C, Zhang Q, Zhao M, et al. Nitrogen-doped aligned carbon nanotube/graphene sandwiches: Facile catalytic growth on bifunctional natural catalysts and their applications as scaffolds for high-rate lithium-sulfur batteries[J]. Adv Mater, 2014, 26: 6100-6105.

[43] Niu S Z, Lv W, Zhou G M, et al. N and S co-doped porous carbon spheres prepared using L-cysteine as a dual functional agent for high-performance lithium-sulfur batteries[J]. Chem Commun, 2015, 51: 17720-17723.

[44] Zhou G M, Zhao Y B, Manthiram A. Dual-confined flexible sulfur cathodes encapsulated in nitrogen-doped double-shelled hollow carbon spheres and wrapped with graphene for Li-S batteries[J]. Adv Energy Mater, 2015, 5: 1402263.

[45] Huang J Q, Zhang Q, Wei F. Multi-functional separator/interlayer system for high-stable lithium-sulfur batteries: Progress and prospects[J]. Energy Storage Mater, 2015, 1: 127-145.

[46] Aurbach D, Pollak E, Elazari R, et al. On the surface chemical aspects of very high energy density, rechargeable Li-sulfur batteries[J]. J Electrochem Soc, 2009, 156: A694-A702.

[47] Huang J Q, Zhang Q, Zhang S M, et al. Aligned sulfur-coated carbon nanotubes with a polyethylene glycol barrier at one end for use as a high efficiency sulfur cathode[J]. Carbon, 2013, 58: 99-106.

[48] Kim K H, Jun Y S, Gerbec J A, et al. Sulfur infiltrated mesoporous graphene-silica composite as a polysulfide retaining cathode material for lithium-sulfur batteries[J]. Carbon, 2014, 69: 543-551.